UCRL-91565
PREPRINT

The Experimental High Pressure Equation of State of a Very Fast Burning Gun Propellant

Marc Costantino
and
Donald Ornellas

JANNAF Combustion Mtg.
Laurel, Maryland
October 1-5, 1984

September 1984

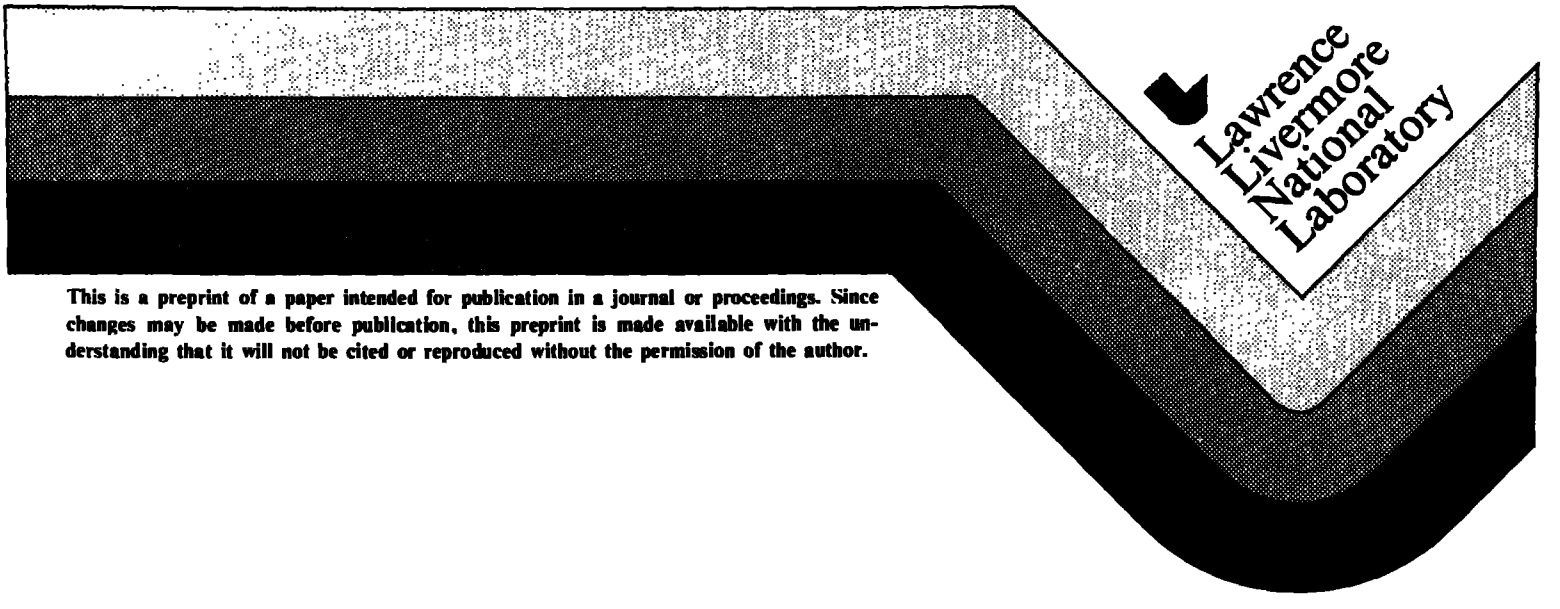

The Experimental High Pressure Equation of State of a Very Fast Burning Gun Propellant

Marc Costantino and Don Ornellas

Lawrence Livermore National Laboratory
Livermore, CA 94550

We present experimental data on the pressure-volume, compressional and shear wave speeds, and failure strength of an 88% TMD, very fast burning gun propellant. The measurements are carried out in the range 0.1 - 400 MPa at a stress rate of 0.1 MPa/sec and at room temperature. The mechanical EOS is dominated by the elastic-plastic response of the pore structure, although precise analysis is complicated by viscoelastic effects with time constants comparable to experimental times. These measurements represent some of very few experimental data available for constitutive relations, and the need for other laboratories to undertake similar experiments is emphasized.

INTRODUCTION

The life of a single propellant grain during the interior ballistic cycle is complicated and exciting. It begins at one atmosphere and some ambient temperature between -50 and 65°C with a set of chemical and physical properties developed during processing, storage, and handling. During ignition and combustion the stress experienced by the grain varies from a simple hydrostatic field created by combustion products flowing around it to the triaxial field present during collision with or confinement by other grains or internal boundaries of the gun. At the same time the temperature varies rapidly, creating an additional, thermally induced, stress. Overlayed on this are other, random, processes such as flame propagation along internal surfaces created by cracks in the grains, variations in the grain geometry, and a highly variable permeability through the packed bed. Only the recent development of computer codes to handle the equations of turbulant fluid mechanics and the conservation and constitutive equations of mechanical modeling has made a theoretical approach to this life possible. Thus it's not surprising that there have been no systematic laboratory studies designed to characterize completely the mechanical equation of state (EOS) of a propellant at the conditions of the interior ballistic cycle.

Such a study would provide for the modeler the surface $G(\sigma(r),T(r),t)$, where G is the set of compliances that relates the deformation of the solid to the stress at a temperature, T, and time t at a point r of the solid. This surface usually is written in several unconnected parts defined by assumed boundary conditions. For example, when the propellant grain is surrounded by gaseous combustion products, it sees a hydrostatic stress field ($\sigma_{ij} = P$, $i = j$; $\sigma_{ij} = 0$, $i \neq j$; $i,j = 1,2,3$) and the compliance matrix reduces to an effective bulk modulus $G_{ij}(P)=K(P)= - V_o\, dP/dV$, $i = j$; $G_{ij} = 0$ $i \neq j$. When the grain strikes the base of the projectile, the stress state is biaxial, with $\sigma_1 > \sigma_2 = \sigma_3 = P$ (in the principal stress frame of reference) and a maximum shear stress can be defined as $\tau_m = (\sigma_1 - \sigma_3)/2$. If this τ_m is sufficiently large (where "sufficiently" depends on the gas pressure around the grain, the temperature, and the time), the grain will fail and, if the failure mode is brittle, will fragment. If the grain is constrained by point or surface contacts with neighboring grains, as in a packed bed, the stress state is even more complicated (triaxial, with $\sigma_1>\sigma_2>\sigma_3$) and the τ_m for failure may be different than for the biaxial case. If the propellant is consolidated and confined by the boundary of the cartridge case, a global boundary condition of zero radial strain applies, and another part of the surface G is required. On top of all this is the movement of G owing to the temperature (e.g., the failure mode may change from brittle to ductile if the temperature increases) and strain rate (e.g., the τ_m to cause failure at a given pressure may increase with strain rate). Addition of the physics necessary to permit non-linear stress waves to become shocks and the chemistry to permit combustion to progress to deflagration and detonation means, simply, that the lot of the interior ballistics theorist is hard.

There has not been much help from the experimentalist. In addition to the usual quickness, dP/dt, and regression, dx/dt (1), data there are, sometimes, results from other tests such as the shotgun test (2,3), the drop weight test (4), high strain rate test (5), and the packed bed loading test (6,7). None of these, however, offer well-characterized data at ($\sigma(r)$,T(r),t) that are required to come up with useful compliances G. This situation still prevails. There are data that span part of the (σ,T,t) field, such as the ($\sigma_1 > \sigma_2 = \sigma_3 = 0.1$ MPa, T, t) failure data of Pinto et. al., (8), of Lieb and Rocchio (9), and of Nicolaides, et. al. (10), and the ($\sigma_1 = \sigma_2 = \sigma_3 > 0.1$ MPa, T=25°C, t) data of Costantino (11,12). However, there is no gun propellant with an adequate data base to provide G for the range of conditions spanned by the interior ballistic cycle.

This paper is a description of part of an on-going program to attempt to define G for a single very high burning rate propellant. The formulation is one of a series comprising a family known

Table 1. Composition of the formulation 1086-7B.

The Theoretical Maximum Density is 1.426 Mg/M^3 (14).

Triaminoguanidine Nitrate	84.55%
Polyethylene Glycol	5.00%
Decarborodecahydride	10.45%

as Hivelite (13), made by the Teledyne-McCormick-Selph Co., Hollister, CA. Compositional details are given in Table 1. In the proposed gun configuration for this propellant, the consolidated charge is attached to the base of the projectile and is constrained radially by the casing wall. The free surface of the grain is ignited and a planar burn propagates along its length. The burn rate is slow (~cm/sec) until an abrupt transition occurs to a new rate of >100 m/sec (Fig 1.) Juhasz, et. al., (15) measured the quickness and Fisher (16) the burn characteristics. Kooker and Anderson have been using these and Costantino's (11,12) data to attempt to model the combustion of this complicated material (17&18).

In previous work in this laboratory (11,12) two formulations (1086-8A and 1086-7B) having ~95% TMD were used to obtain hydrostatic pressure-volume, compressive loading with a zero radial strain boundary condition, and compressional and shear wave sound speeds on increasing pressure to 200 MPa (29000 PSI). The present work is an extension of that effort. The pressure range has been increased to 400 MPa and, using a bellows piezometer, hydrostat data have been obtained for both increasing and decreasing pressure. Compressional and shear sound wave speeds, and the failure curve are reported. Since a major objective of this program is to provide a consistent, complete set of mechanical EOS data for use in modeling, all of the experiments were carried out, as nearly as possible, at the same temperature (T=25±1°C) and at the same stress rate (0.1 MPa/s). The latter is particularly important, in view of the time dependent effects found in the 95% TMD material (11). Future work will focus on the mechanical properties at strain rates from 10^{-2} s^{-1} to 10^{2} s^{-1}.

SAMPLES

The 1086-7B samples were pressed to 88% TMD at Teledyne-McCormick-Selph in April 1983 and stored in cardboard cannisters until use. The samples were 1.27 cm in diameter and 2.54 cm in length, with densities (by geometry) shown in Table 2. No further sample preparation was done, with the exception of removing pits in the ends (caused by particle pull-out during removal from the pressing die) by polishing on 600 grit silicon carbide paper with Freon TF lubricant. The results of safety tests for the 95% TMD material reported in Ref. 11 were assumed to apply to the 88% TMD material.

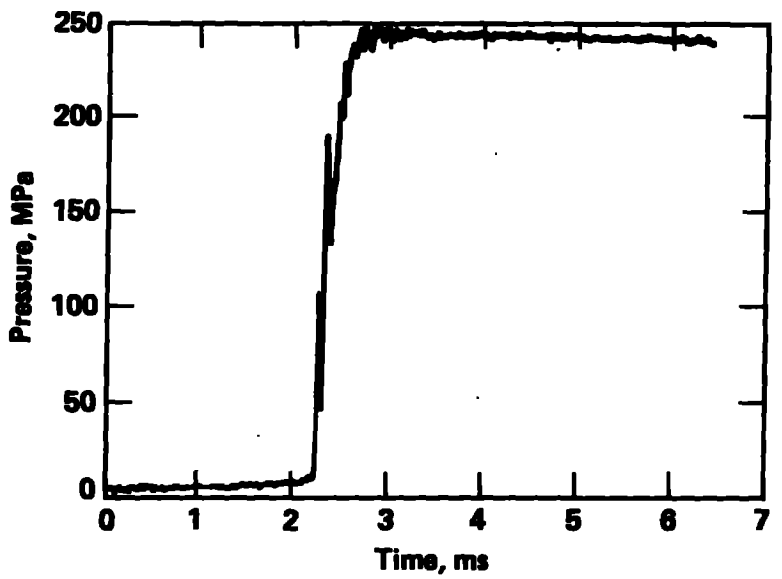

Figure 1. A Pressure-time trace in a closed-bomb experiment, showing the transitions in burn rates (Ref. 15).

HYDROSTAT

Method

The hydrostat relative to the equation of state of water was measured using a bellows piezometer, shown schematically in Fig. 2. This classic approach (19-21) to P-v measurements was chosen in order to obtain reliable data on decreasing pressure. In this method, the sample assembly is placed in the bellows body, evacuated, the remaining volume filled with deionized, deaereated water, and the plug and cap assembled to seal the piezometer. Careful weighing (to 0.0001 gm) of the various components gives the total weight of the water in the piezometer. The guide, a finely machined cylinder that fits closely the linear bearing without binding, is attached to the bellows body and inserted into the bearing. The bellows body is secured to the frame with set screws, so that the displacement of the bellows relative to the frame can be measured by the motion of the Be-Cu wiper arm along the fixed wire of the potentiometer, a 5 cm length of 30 gauge Tophet-A. The absolute volume of the piezometer is related to its linear displacement by filling it with water and measuring

$$[u(P)/u_0(P) - u(0.1\ \text{MPa})/u_0(0.1\ \text{MPa})] = \Delta(u/u_0),$$

where $u(P)$ and $u_0(P)$ are the voltages at pressure P across the variable and fixed arms of the potentiometer, respectively. The associated volume of water at

Table 2. Densities (TMD = 1.426 Mg/M^3)

Sample	Density (Mg/M^3)
PV7B11	1.246
PV7B12	1.246
PV7B13	1.255
PV7B14	1.255
PV7B15	1.253
PV7B16	1.255
PV7B17	1.251
PV7B18	1.256

P is calculated using the EOS described below, and the $[\Delta V(P) - \Delta(u/u_0)]$ pairs least squares fitted to a quadratic:

$$\Delta V(cm^3) = a_1\ [\Delta(u/u_0)] + a_2\ [\Delta(u/u_0)]^2 \qquad (1)$$

The volume of the piezometer, V_p, at P=0.1 MPa and T = room temperature is found using the weights and densities of the various components:

$$V_p\ (0.1\ \text{MPa}) = V_w + V_e + V_a + V_j + V_s, \qquad (2)$$

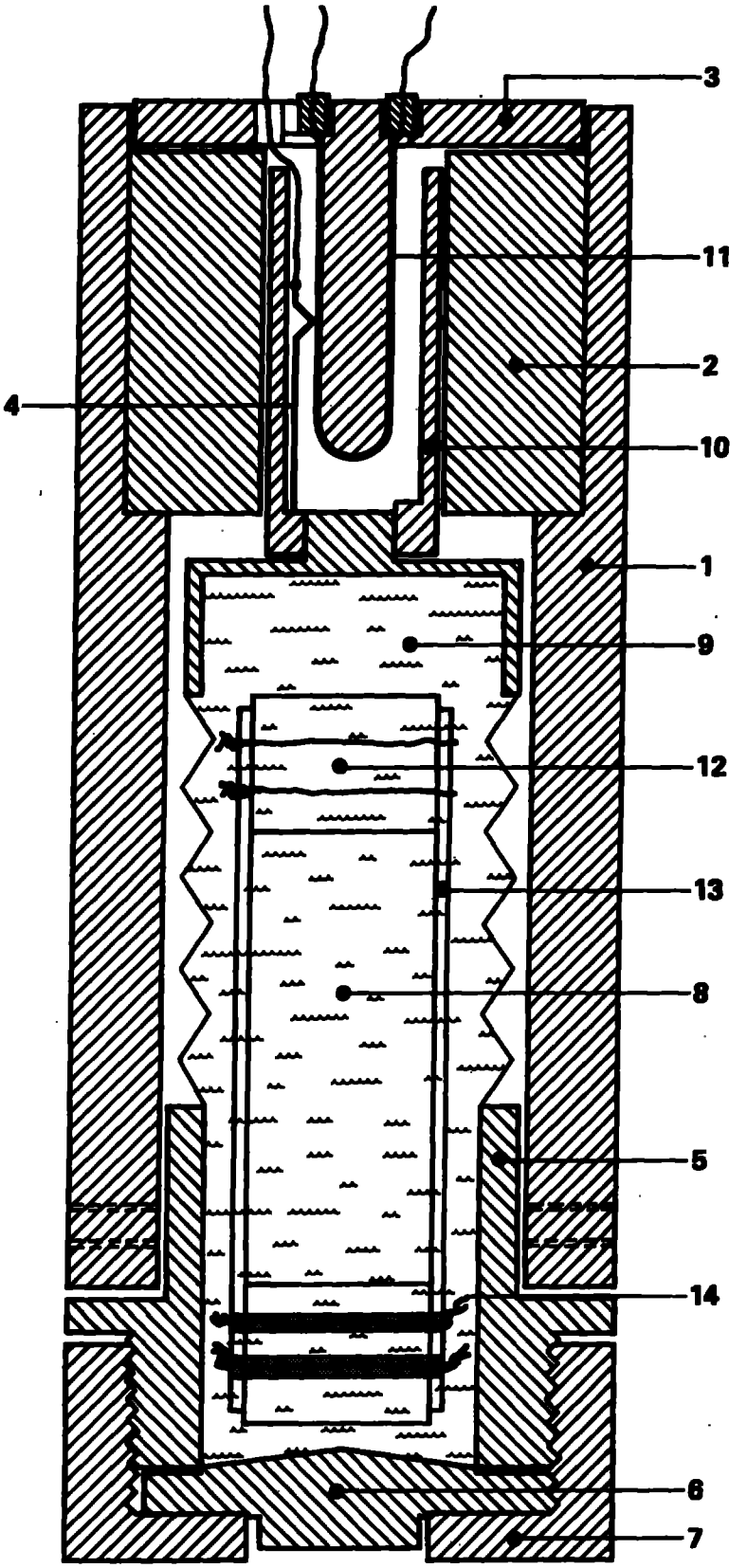

Figure 2. The bellows piezometer. 1) Frame; 2) Linear bearing; 3) Linear potentiometer assembly; 4) Wiper arm; 5) Body; 6) Plug; 7) Cap; 8) Sample; 9) Water; 10) Guide; 11) Potentiometer fixed wire; 12) Endpiece; 13) Jacket; 14) Wire to secure the jacket to the endpiece.

where the subscripts w, e, a, j, and s refer to water, end pieces, wires, jacket, and sample, respectively. Finally, the volume at P is

$$V_p = V_p\ (0.1\ \text{MPa}) + \Delta V_p \tag{3}$$

and the volume of the sample at P is:

$$V_s(P) = V_p(P) - [V_w(P) + V_e(P) + V_a(P) + V_j(P)] \tag{4}$$

$$= V_p\ (0.1\ \text{MPa}) + \Delta V_p - [V_w(P) + V_e(P) + V_a(P) + V_j(P)].$$

Volumes of the water and sample addenda are found from their respective EOSs. The EOS of water at T=23°C was constructed using the data of Kennedy, et. al., (22) for P<110 MPa and of Burnham, et. al. (23) for P>110 MPa. These data were fitted to a cubic polynomial over the range 0 - 400 MPa, giving residuals of the order of 10^{-4} cm^3. The fitting parameters were used over the entire temperature range of the experiments (23°C<T<26°C), since their change with temperature results in errors small compared to others present in the experiment. The EOS of water used in this work is

$$V_w(P) = V_w(P=0.1\ \text{MPa}, T)[1. + \rho_0(a_1\Delta P + a_2\Delta P^2 + a_3\Delta P^3)], \tag{5}$$

where $\Delta P = P - 0.1$, $a_1 = -4.4031(10)^{-4}$, $a_2 = 5.8267\ (10^{-7})$, and $a_3 = -4.6099\ (10^{-10})$. ρ_0 is the absolute density of water at (P=0.1, T) from Ref. 24.

The EOS of the polyolefin heat-shrinkable tubing used as the jacket material was determined in a separate experiment to be:

$$V_j(P) = V_j(0.1)[1. + a_1\Delta P + a_2\Delta P^2] \tag{6}$$

where $a_1 = -2.0044\ (10^{-4})$ and $a_2 = 1.0437\ (10^{-8})$ for increasing pressure; and $a_1 = -3.3939\ (10^{-4})$ and $a_2 = 3.6162\ (10^{-7})$ for decreasing pressure. The density at ambient conditions, measured by geometry, is 0.92 Mg/m^3.

The EOS of the 316 stainless steel used in the endpieces, V_e, and wires, V_a, was taken as:

$$V_{e,a}(P) = V_{e,a}\ (0.1)[1. - \Delta P/K] \tag{7}$$

where $K = 1.63\ (10^5)$ MPa.

Pressure was measured using a manganin gauge inside the pressure vessel, and is accurate to 0.5 percent. Although the temperature was not measured during the experiment, the relatively slow rate in the change of pressure, together with the large thermal mass of the pressure fluid and vessel, resulted in temperatures close to that measured before each experiment. A typical experiment lasted about 2 1/2 hours.

All voltage measurements were made using an HP 3497A Data Acquisition System linked to an LSI 11/23 microcomputer.

ERRORS

While a complete error analysis of this method is not complicated (25), it is tedious, so only a summary will be given. Estimates of probable error show that the major sources are (in relative order of importance) calibration of the piezometer volume against its linear displacement, component EOSs, and initial measurements. These total about 0.07cm^3, resulting in a maximum probable error of ~0.4% in total volume and ~15% in $\Delta V/V_0$ of the sample. That this is an overestimate is apparent from Fig. 3, which shows the results of a standard experiment.

During the course of this work, five standard experiments were made in order to check the consistency of the measurements and data reduction with respect to the EOS of water and to detect possible changes in the piezometer. A standard experiment differed from a sample experiment only in that the propellant sample was replaced by a "sample" of water having the same dimensions. (In practice, after a sample experiment was made, the sample was removed from the sample assembly by cutting open the jacket; then the jacket, endpieces, and wires were replaced in the piezometer with the original volume of the propellant sample being replaced by water). If there were no errors in calibration, component EOS (other than water), or initial measurements, the "experimental" water EOS should agree with Eqn. 5. As Fig. 3 shows, the deviations are considerably less than 15% of $\Delta V/V_0$. The error in $\Delta V/V_0$ is estimated to be about 5%.

HYDROSTAT RESULTS

Nine hydrostat experiments were made and one, PV7B19, discarded owing to equipment malfunction. Approximately 400 pressure-voltage data points were taken on increasing and on decreasing pressure, at intervals of 10 sec or 1.0 MPa. One hundred points, approximately equally spaced in pressure, were selected from each curve and fitted using a least squares cubic spline with variable knots algorithm (26). In this method, the number of knots, or the points at which the splines and their derivatives are matched, is specified over the range of the independent variable. The knots at the ends of the interval are fixed, and those between are adjusted to give the best least squares fit. The number of knots is chosen so that the residuals of the fit are of the same order as the precision of the data. The increasing pressure data were fitted using 4 knots and the decreasing pressure data with 3. The hydrostat for each sample, then, is described by a set of n-1 cubic equations, where n is the number of knots used. The volume compression, $-(V-V_0/V_0)$, for the interval i is calculated from:

$$-(V-V_0)/V_0 = a_{i_0} + a_{i_1}\Delta P + a_{i2}\,\Delta P^2 + a_{i_3}\,\Delta P^3 \qquad (8)$$

where $\Delta P = (P - P_i)$, $P_i < P < P_{i+1}$ and the coefficients a_{ij} and the location of the knot, P_i, for each experiment are in Table 3. An example of the data and fitted curves is shown in Fig. 4.

Reduction of the sound speed data in the following section requires the length of the sample as a function of pressure. This is obtained by defining an average hydrostat $(\Delta V/V_0)$ avg and, assuming isotropic compression,

$$L(P) = L\,(0.1)\,[1. - (1/3)\,(\Delta V/V_0)\ \text{avg})] \qquad (9)$$

The average hydrostat was found by averaging the volume compressions for the 8 experiments, using the coefficients of Table 3. The 100 points equally spaced in pressure for increasing and for decreasing pressure were fitted, yielding the coefficients given at the bottom of Table 3 and the curve in Fig. 5. The error bars represent one standard deviation in the average $\Delta V/V_0$.

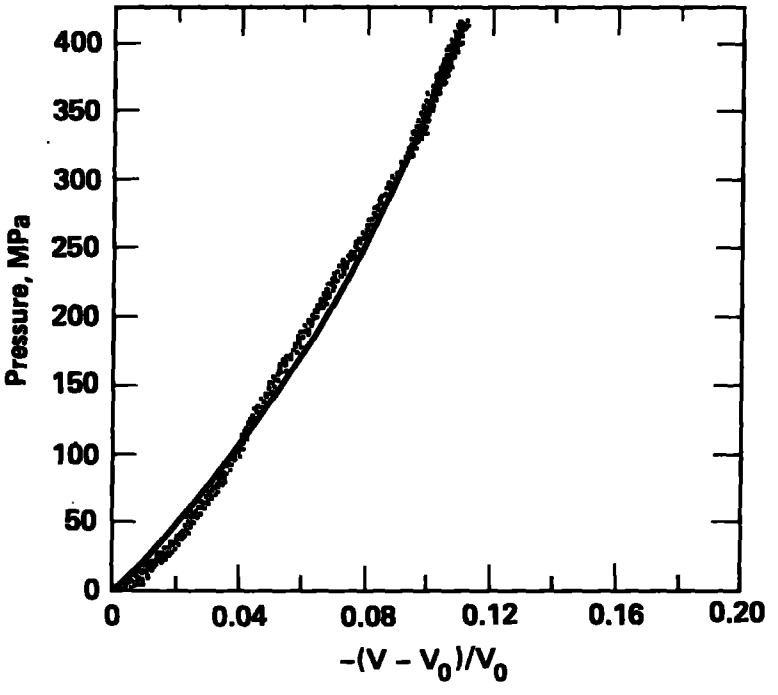

Figure 3. Results of a standard experiment. If the experiment were perfect, the data for the EOS of water would lie on the curve (Equ. 5).

EXPERIMENT	RANGE	A0	A1	A2	A3
PV7B11	0.1 ≤ P ≤ 176.8	9.8861E-03	1.3214E-04	5.4918E-06	-1.6384E-08
	176.8 ≤ P ≤ 224.4	1.1425E-01	5.3821E-04	-5.1937E-06	1.4339E-08
	224.4 ≤ P ≤ 450.0	1.3414E-01	3.3172E-04	-1.1479E-06	1.2802E-09
	0.1 ≤ P ≤ 210.8	1.3847E-01	1.5254E-04	-5.6114E-07	-1.2488E-09
	210.8 ≤ P ≤ 450.8	1.5570E-01	8.7861E-05	2.1965E-07	-1.8429E-09
PV7B12	0.1 ≤ P ≤ 156.2	2.7840E-03	-3.2378E-05	8.8935E-06	-2.8162E-08
	156.2 ≤ P ≤ 210.8	1.0419E-01	6.6546E-04	-4.2948E-06	7.1051E-09
	210.8 ≤ P ≤ 450.8	1.3116E-01	3.8469E-04	-8.4485E-07	-1.6138E-10
	0.1 ≤ P ≤ 206.1	1.3779E-01	2.4647E-04	-1.1724E-06	3.6151E-09
	206.1 ≤ P ≤ 450.8	1.6171E-01	9.6569E-05	4.4394E-07	-3.1823E-09
PV7B13	0.1 ≤ P ≤ 99.5	4.3962E-03	-6.6320E-05	1.5123E-05	-6.4582E-08
	99.5 ≤ P ≤ 312.0	8.3774E-02	-1.0260E-03	-4.1320E-06	9.3891E-09
	312.0 ≤ P ≤ 450.8	1.2691E-01	-5.4721E-06	-2.3111E-07	7.1628E-09
	0.1 ≤ P ≤ 78.5	1.1476E-01	-4.4268E-04	-6.7844E-06	3.4002E-08
	78.5 ≤ P ≤ 450.8	1.3416E-01	-7.8255E-06	3.9411E-07	-7.2449E-10
PV7B14	0.1 ≤ P ≤ 99.8	8.1022E-03	-2.6102E-04	2.1420E-05	-1.0125E-07
	99.8 ≤ P ≤ 269.5	8.4218E-02	1.1348E-03	-8.1985E-06	1.1372E-08
	269.5 ≤ P ≤ 450.8	1.2565E-01	1.1680E-04	2.2627E-07	-4.4998E-09
	0.1 ≤ P ≤ 176.9	1.2588E-01	1.4868E-04	-1.2063E-06	3.4911E-09
	176.9 ≤ P ≤ 450.8	1.6234E-01	4.1491E-05	6.4515E-07	-2.6745E-09
PV7B15	0.1 ≤ P ≤ 101.8	4.0821E-03	-1.3842E-04	-1.7457E-05	-7.7907E-08
	101.8 ≤ P ≤ 242.3	9.0389E-02	1.0389E-03	-6.0476E-06	1.3049E-08
	242.3 ≤ P ≤ 450.8	1.5319E-01	1.1192E-04	-5.3717E-07	2.2358E-09
	0.1 ≤ P ≤ 147.1	1.4713E-01	2.3377E-04	-1.2484E-06	3.6469E-09
	147.1 ≤ P ≤ 450.8	1.5733E-01	2.6982E-05	5.4135E-07	-1.8307E-09
PV7B16	0.1 ≤ P ≤ 183.2	2.3681E-03	-3.7454E-05	1.6654E-05	-7.4509E-08
	183.2 ≤ P ≤ 231.2	7.3867E-02	1.0209E-03	-6.3884E-06	1.6431E-08
	231.2 ≤ P ≤ 450.8	1.5434E-01	1.9303E-04	-7.2681E-08	-1.2004E-09
	0.1 ≤ P ≤ 243.1	1.5444E-01	2.2804E-04	-1.0442E-06	1.9225E-09
	243.1 ≤ P ≤ 450.8	1.7378E-01	8.1090E-05	3.5712E-07	-3.7225E-09
PV7B17	0.1 ≤ P ≤ 114.5	8.1232E-04	-4.4932E-04	1.7435E-05	-7.7757E-08
	114.5 ≤ P ≤ 203.9	8.7877E-02	9.2053E-04	-7.1550E-06	2.5173E-08
	203.9 ≤ P ≤ 450.8	1.5254E-01	2.1280E-04	-1.1995E-06	2.7021E-09
	0.1 ≤ P ≤ 210.8	1.1212E-01	2.3031E-04	-1.2352E-06	2.7304E-09
	210.8 ≤ P ≤ 450.8	1.3836E-01	7.2676E-05	4.8416E-07	-2.7400E-09
PV7B18	0.1 ≤ P ≤ 126.1	6.4221E-04	2.5023E-04	3.6973E-06	-3.8362E-08
	126.1 ≤ P ≤ 247.6	1.0534E-01	8.6674E-04	-4.8047E-06	1.0309E-08
	247.6 ≤ P ≤ 450.8	1.6226E-01	1.5574E-04	-1.0474E-06	3.4309E-09
	0.1 ≤ P ≤ 210.8	1.3525E-01	2.9027E-04	-1.8590E-06	3.8312E-09
	210.8 ≤ P ≤ 450.8	1.6770E-01	1.6231E-05	5.5348E-07	-2.1824E-09
AVERAGE	0.1 ≤ P ≤ 109.8	-2.1232E-04	-5.2886E-05	1.3692E-05	-5.5959E-08
	109.8 ≤ P ≤ 251.7	8.4842E-02	9.3124E-04	-4.7173E-06	9.5849E-09
	251.7 ≤ P ≤ 450.0	1.4940E-01	1.7140E-04	-2.3522E-07	8.7959E-10
	0.1 ≤ P ≤ 184.4	1.3270E-01	2.1342E-04	-1.2289E-06	3.1189E-09
	184.4 ≤ P ≤ 450.0	1.5448E-01	5.2902E-05	4.2681E-07	-1.9649E-09

Table 3. Knot locations and coefficients for the cubic spline fits to the hydrostat data.

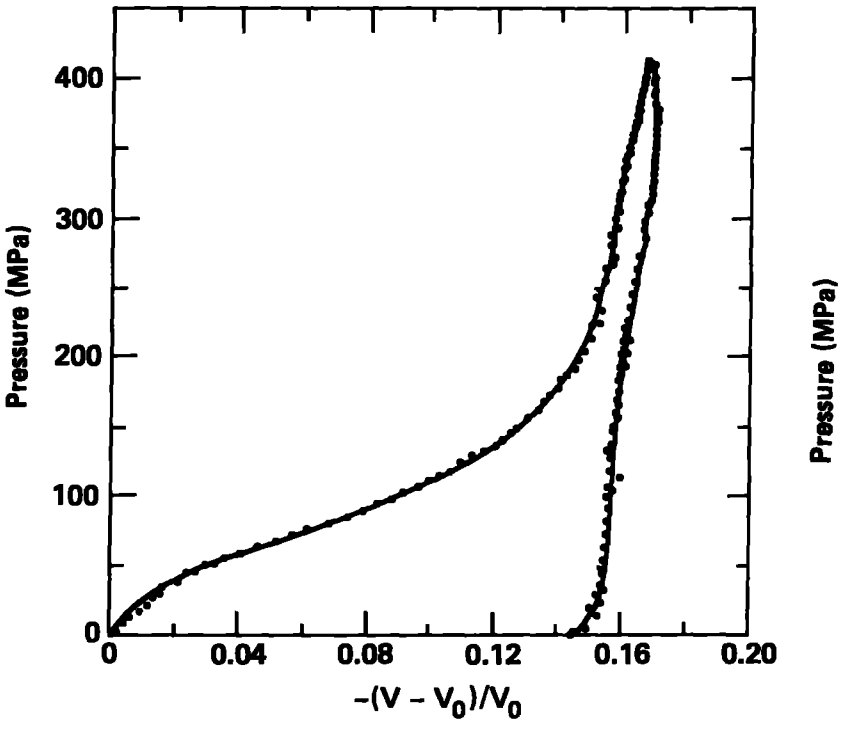

Figure 4. Results for a typical hydrostat experiment. The solid curve is the fitted cubic spline.

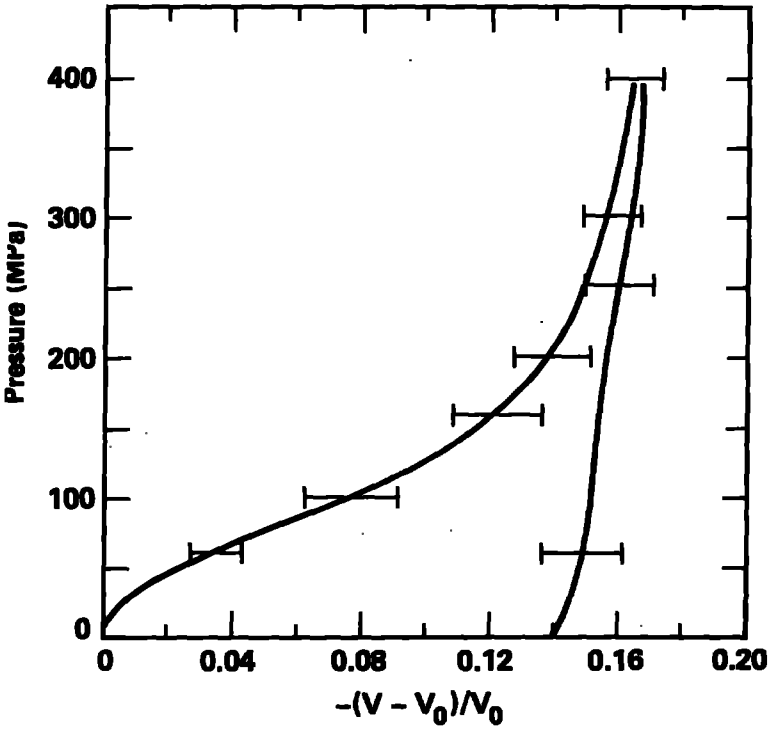

Figure 5. The average hydrostat for 88% TMD 1086-7B. The error bars are one standard deviation.

SOUND SPEEDS

The compression and shear wave sound speeds were measured using the time of flight technique described in Ref. 11, with the exception that only shear polarized transducers were employed. Previous experiments demonstrated that enough energy was transmitted as a P-wave to provide a good signal, and that the P-wave arrival times measured using P- and S- wave transducers were the same within the time resolution of the experiment. The schematic of the measurement system and a typical signal are shown in Fig. 6. The pressure was increased at a rate of 0.1 MPa/sec, as in the hydrostat experiment. The system delay time, t_d, was assumed the same as in Ref. 11, since no changes were made in the apparatus.

The sound speeds were calculated from:

$$U(P) = L(P)/[t_a - t_d] \qquad (10)$$

where t_a is the measured arrival time and L(P) is the length of the sample at pressure P, calculated from the average hydrostat. The data are presented in Figs. 7 and 8, and in Table 4.

Table 4. Average Values for the Compressional (U_p) and Shear (U_s) Sound Speeds for 88% TMD 1086-7B

P(MPa)	U_p(km/s)	U_s(km/s)
0.1	2.29	1.17
20	2.35	1.20
40	2.42	1.22
60	2.49	1.25
80	2.61	1.29
100	2.76	1.34
120	2.91	1.38
140	3.11	1.41
160	3.18	1.45
180	3.30	1.47
200	3.43	1.50
220	3.51	1.52
240	3.59	1.54
260	3.66	1.55
280	3.71	1.56
300	3.76	1.57
320	3.79	1.58
340	3.86	1.59
360	3.90	1.60
380	3.93	1.61

FAILURE CURVE

The failure curve, shown in Fig. 9, is used to separate the states of compressive stress which a solid can sustain without failing and those which result in failure. (An introductory discussion of strength and failure can be found in Ref. 27.) A right circular cylinder is loaded under biaxial stress, with the principal stresses

$$\sigma_1 > \sigma_2 = \sigma = {}_3 = \sigma_c.$$

The maximum principal stress, σ_1, is the axial load; and the intermediate and minimum principal stresses, $\sigma_2 = \sigma_3 = \sigma_c$, the confining pressure. The experiment is shown schematically in Fig. 10, and consists of following the stress path shown by the dotted line in Fig. 9. The pressure around the jacketed sample is raised to σ_c, after which an additional axial load is applied by advancing the piston into the pressure vessel, keeping σ_c constant.

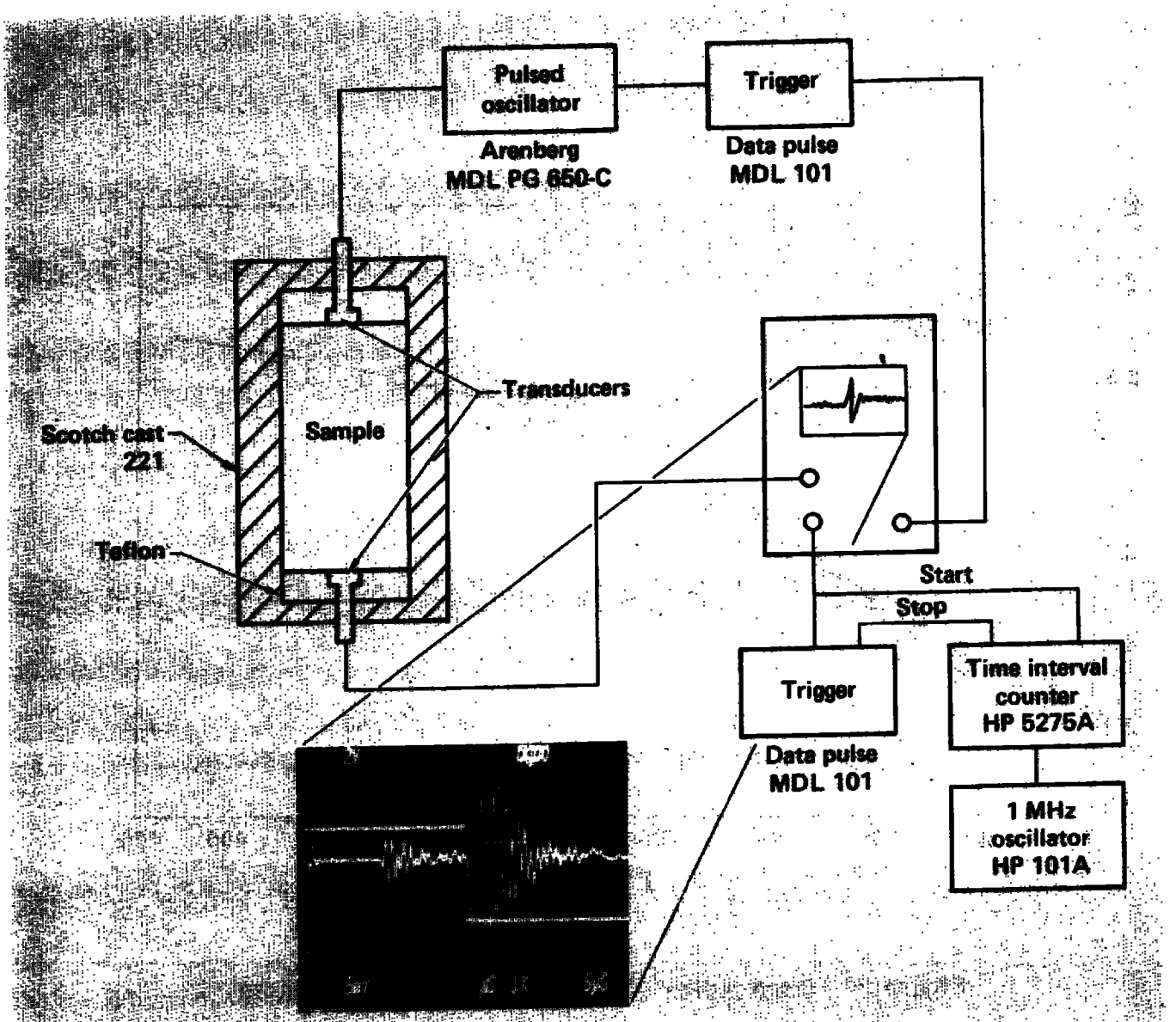

Figure 6. Schematic of the sound speed measurement.

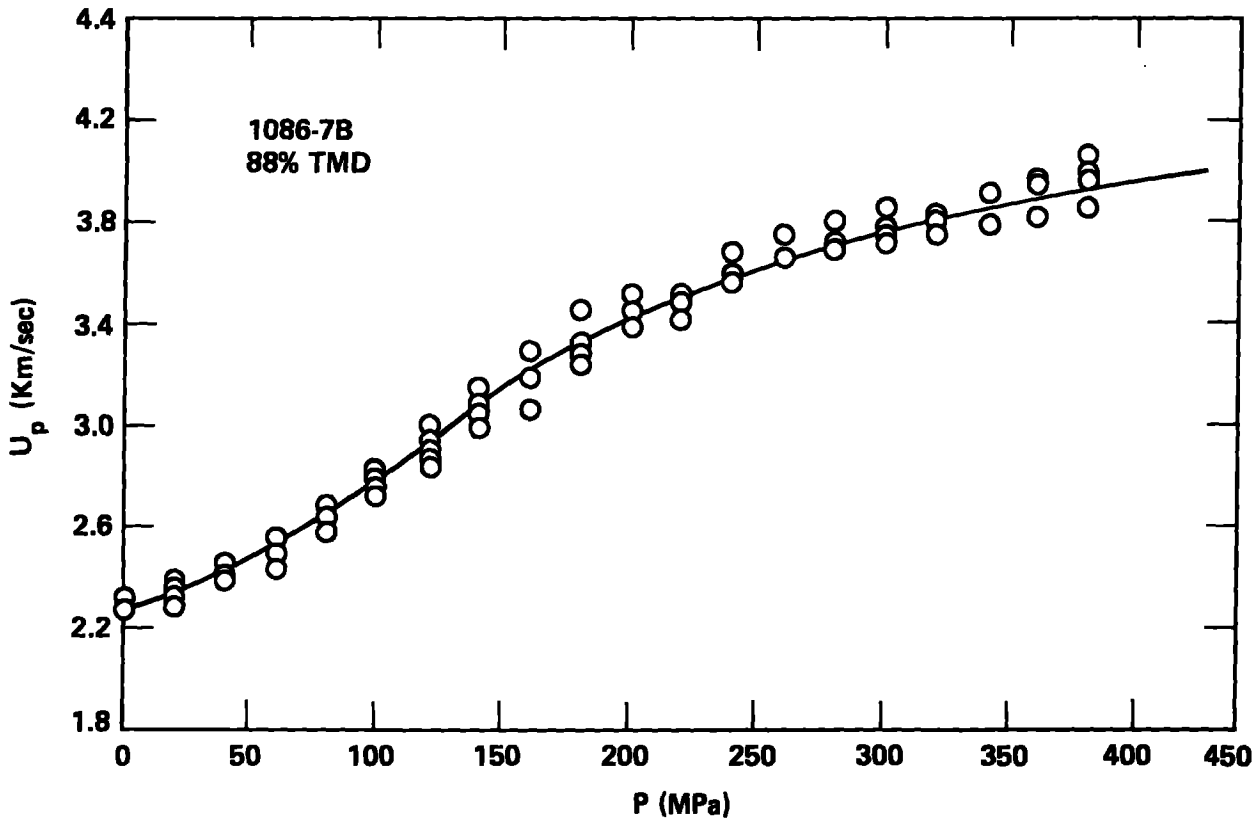

Figure 7. Compression wave speed for 88% TMD 1086-7B.

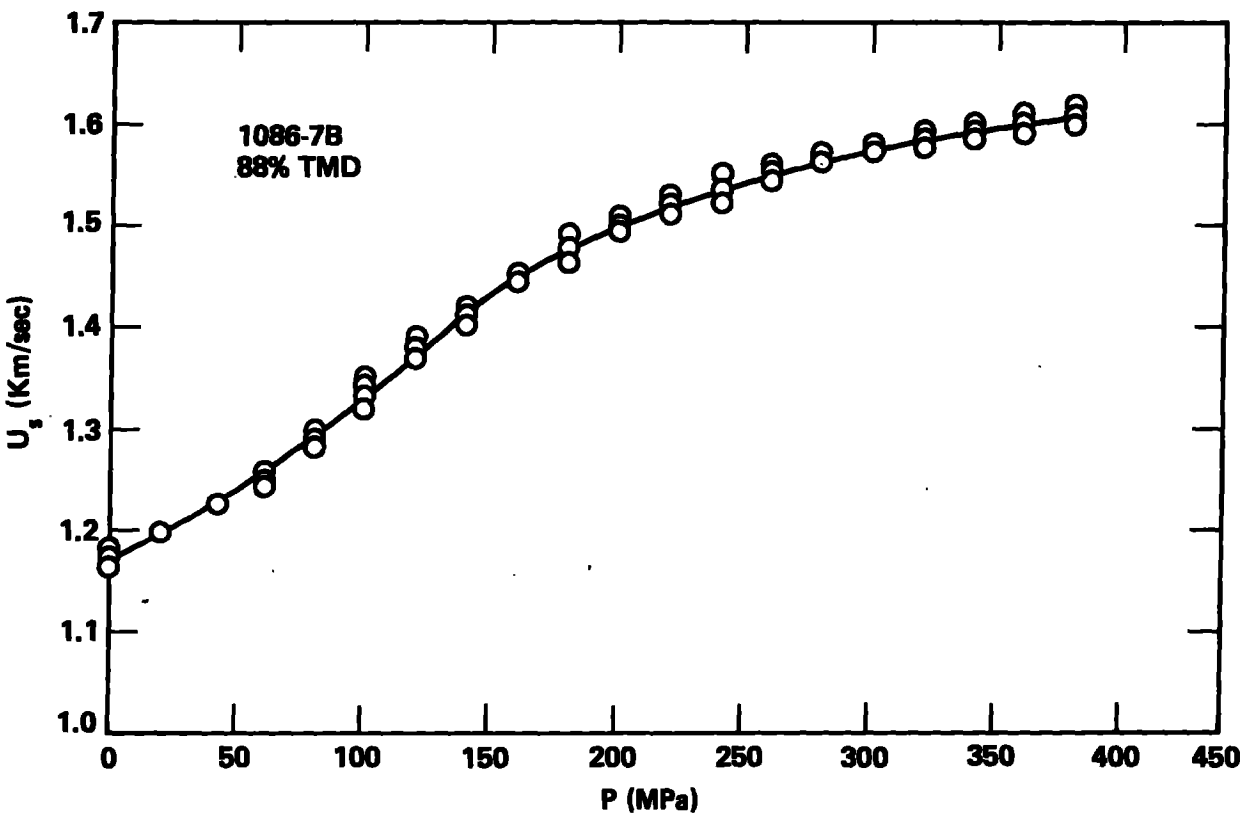

Figure 8. Shear wave speed for 88% TMD 1086-7B.

The axial stress-axial strain diagram is shown in Fig. 11. At some point, the solid may lose its ability to sustain an incremental increase in axial load, and it fails. For brittle materials, this point is quite obvious; while for ductile or strain hardening materials the failure point is chosen arbitrarily as the stress at some particular strain, e.g., 3%. The locus of these failure points is the failure curve, which often is plotted as the maximum shear stress, $\tau_m = (\sigma_1 - \sigma_3)/2$ vs. the confining pressure, σ_3. The failure curve often is a strong function of the temperature and the strain rate.

Simple constitutive models typically represent the data with a three parameter curve (either two straight line segments or a quadratic) so usually we choose to measure three points on the curve a statistically significant number of times. One point always is at $\sigma_3 = 0.1$ MPa (the uniaxial point) and the second usually is at the high end of the stress range of interest. The third point is selected near the expected maximum in the curvature of the curve.

Since these are the first data for the compressive failure strength of a gun propellant at confining pressures greater than 0.1 MPa, we choose to do experiments at several confining pressures, concentrating on low values, where we expect most of the action to occur. In this first series of experiments, the failure at room temperature and a strain rate of 10^{-4} s^{-1} is measured. The sample is a right circular cylinder 1.27 cm in diameter and 2.54 cm in length, having ends parallel and flat to .02 mm. Tungsten carbide endpieces and a polyolefin jacket are attached in a way similar to that in the hydrostat experiment, in order to prevent the pressure fluid from intruding into the sample. The sample is placed coaxially with a load cell in the pressure vessel, the pressure increased to σ_c at a rate of 0.1 MPa/s, and an additional axial load applied with the pressure vessel piston. The force on the sample is measured by the load cell, and the sample axial displacement by a linear transducer, corrected for the other compliances in the load chain. The maximum shear stress is calculated using:

$$\tau_m = (\sigma_1 - \sigma_3)/2 = F/2A_0 \qquad (11)$$

where F is the force on the load cell and A_0 is the original sample cross sectional area. A typical $\sigma_1 - \varepsilon_1$ (where $\varepsilon_1 = -(L-L_0)/L_0$; the maximum principal, or axial, strain) is shown in Fig. 11. The effective Young's modulus, $E_{eff} = d\sigma_1/d\varepsilon_1$, is found from the linear part of the curve.

Results for the 88% TMD 1086-7B propellant are shown in Fig. 9 and listed in Table 5. For the 0.1 and 3.0 MPa experiments, the propellant showed a maximum in the axial stress-axial strain curve. As shown in Fig. 11, the failure for the 0.1 point is brittle, i.e., the axial stress decreases abruptly at some strain, in this case about 1%. (Note that, throughout, the axial strains and stresses are "engineering" values; the sample length used to calculate the strain and the sample diameter used to calculate the stress are not corrected for hydrostatic or for biaxial compression). Near 3MPa the failure mode becomes ductile, characterized by a broad maximum in the sustained shear stress, followed by a slight decrease. At higher confining pressures, the material may be said to "work harden", in the sense that the maximum shear stress carried by the propellant increases with axial strain. The 15 and 20 MPa points suggest a plateau in the failure curve, probably related to the beginning of the crush-up of the porosity, demonstrated by a distinct softening in the hydrostat data above 20 MPa (See Fig. 4). For this reason, the data below 20 MPa are joined to the points at 200 and 400 MPa with a dashed line. Further data may very well show a plateau, followed by an increase in strength.

The effective Young's modulus is found from the slope of a straight line, drawn by eye, through the low strain portion of the curve. As is the case normally, there is a fair scatter in these values, but the compaction of the material at confining pressures at 200 and 400 MPa clearly leads to stiffer and stronger material.

These data demonstrate the significant effect of confining pressure on the strength of propellants. During the interior ballistic cycle, individual grains having even moderate gas permeabilities experience a confining pressure owing to combustion products of the igniter and propellant. This means that their strength and failure mode is quite different from that observed at atmospheric pressure. Results from shotgun, drop-weight, or other compression tests at 0.1 MPa

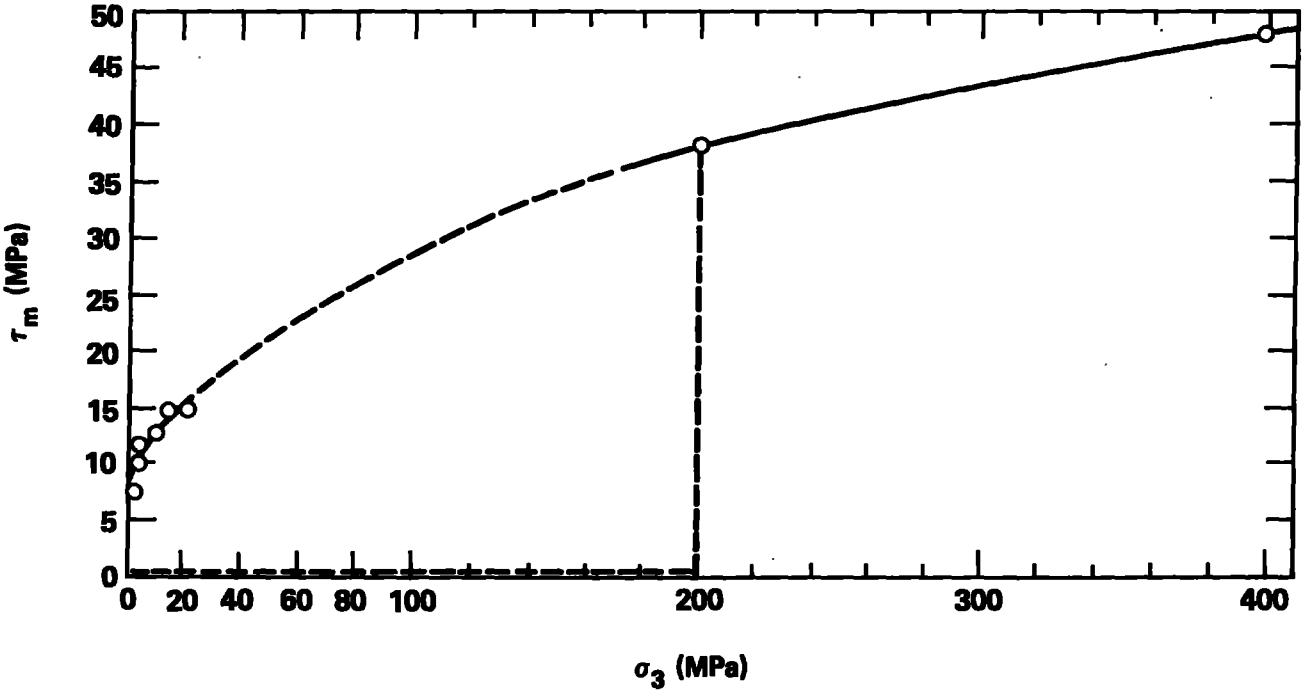

Figure 9. Failure curve for 88% TMD 1086-7B. Each point represents between 3 and 7 experiments, with the scatter falling within the circle. The stress path for the σ_c = 200 MPa point, shown by the dashed line, is hydrostatic (τ_m = 0) to σ_3 = 200 MPa. Then σ_1 is increased with σ_3 constant until the sample fails. These data are for the shear stress at 3% axial strain.

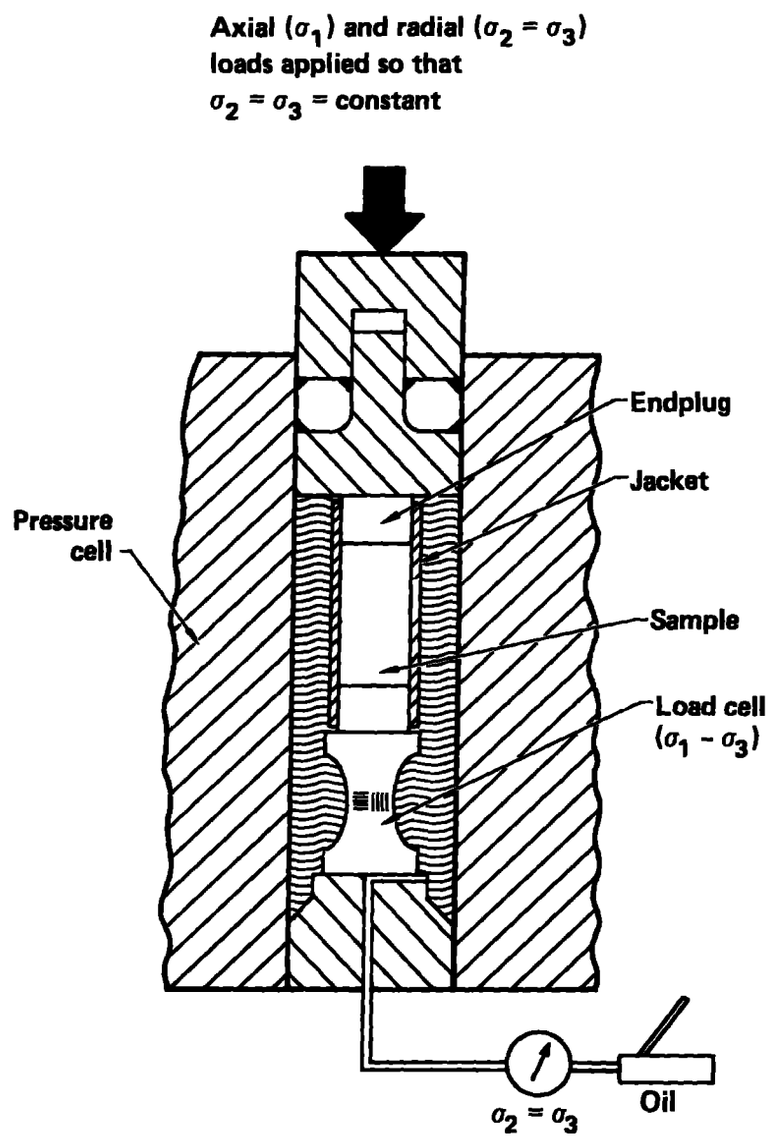

Figure 10. Schematic of the failure curve experiment.

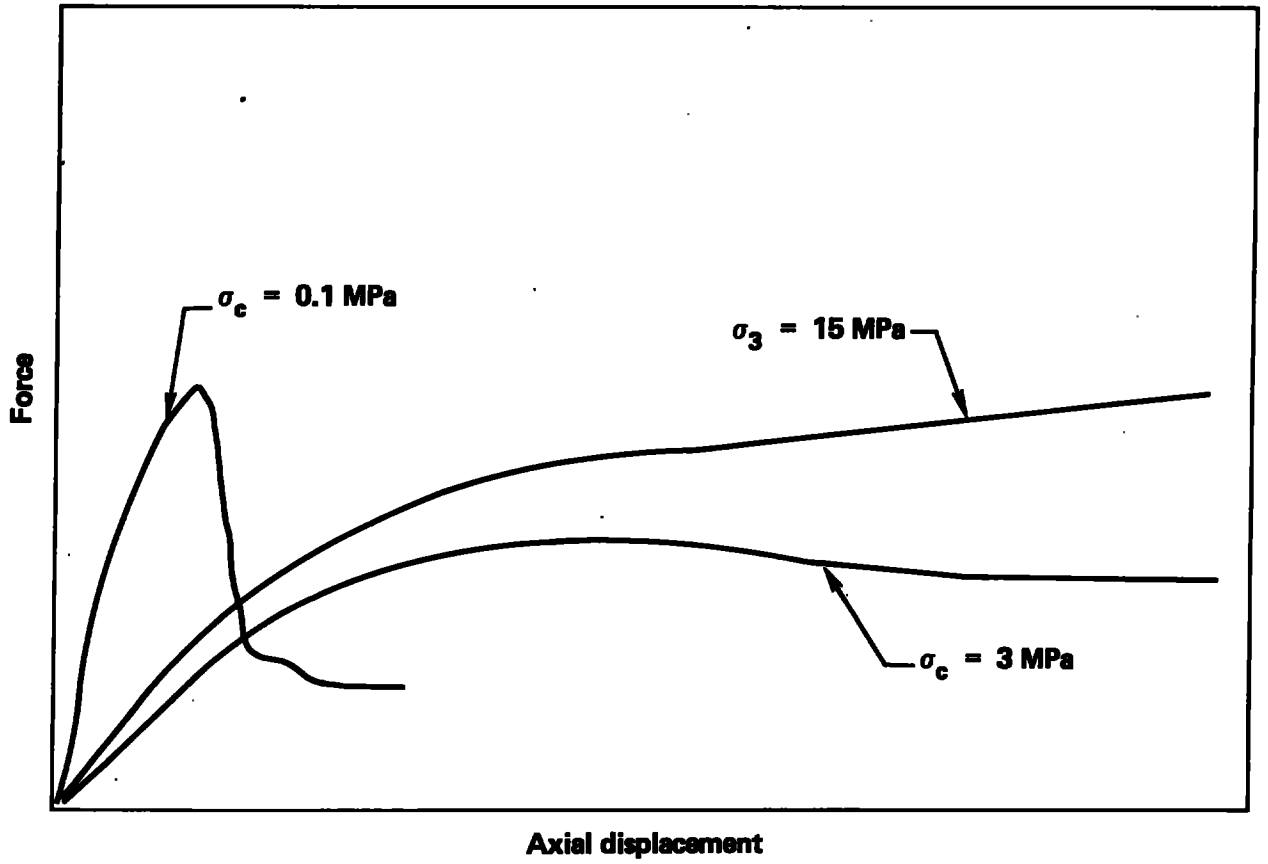

Figure 11. Typical axial force vs axial displacement curves, showing a brittle failure mode at σ_c = 0.1 MPa; ductile failure at σ_c = 15 MPa; and a transition between brittle and ductile at σ_c = 3 MPa.

Table 5. Maximum shear stress at 3% and 5% axial strains at various confining pressures.

Confining Pressure (MPa)	τ_m (MPa) at 3% Axial Strain	τ_m (MPA at 5% Axial Strain	Effective Young's Modulus (GPa)
0.1	8.4[a]	-	-
0.1	8.0	-	-
0.1	7.8	-	-
0.1	7.4	-	-
0.1	7.6	-	-
0.1	7.2	-	-
3.0	10.2[b]	8.7	1.76
3.0	9.9	8.9	2.64
3.0	10.7	8.4	2.37
5.0	11.9	12.1	2.33
5.0	12.5	12.4	2.12
5.0	11.3	11.8	2.13
5.0	11.5	11.9	1.88
5.0	11.2	11.8	1.30
5.0	11.5	11.9	2.69
10.0	12.5	14.0	1.52
10.0	12.7	14.0	1.45
10.0	13.0	14.1	2.05
10.0	12.6	14.1	2.04
10.0	12.9	14.1	1.56
10.0	12.9	14.3	1.97
10.0	12.8	14.5	1.66
15.0	15.0	16.6	2.76
15.0	14.3	16.1	2.67
15.0	14.6	16.3	2.99
15.0	14.6	16.2	2.15
20.0	15.3	17.4	2.92
20.0	14.5	16.6	1.17
20.0	14.9	17.0	3.14
200.0	38.1	43.6	5.10
200.0	37.6	43.3	4.77
200.0	38.5	43.2	5.13
400.0	47.9	55.3	6.48
400.0	48.4	56.3	6.52

(a) Brittle failure near 1% axial strain (b) Maximum strength.

confining pressure probably do not apply to the grain in the gun environment. Even the present results do not give a correct picture, since the strain rates experienced by propellant grains in the ballistic cycle are 4 to 7 orders of magnitude larger than those of this work. Experiments to extend the strain rate to 10^2 S^{-1} at 400 MPa confining pressure are underway.

Acknowledgement

We wish to thank Dr. Wunan Lin and Mr. Stan Trettenero for their assistance in making the hydrostat and sound speed measurements. This work was performed under U.S. Army Ballistic Research Laboratory Project Order BRL PO-281.

This work was perfomed under the auspices of the U.S. Department of Energy by Lawrence Livermore National Laboratory under contract No. W-7405-Eng-48.

References

1. A.A. Juhasz, Ed., "Round Robin Results of the Closed Bomb and Strand Burner", CPIA Publication 361, July 1982.

2. K.B. Isom, R. L. Keefe, and J.H. Thacher, "Standardized Propellant Testing for DDT Potential", 15th JANNAF Combustion Meeting 1978.

3. R.A. Gould, "Progress Report of the JANNAF Panel on Shotgun/Relative Quickness Testing", 1980 JANNAF Propulsion Systems Hazards Subcommittee Meeting, Monterey, CA October 1980. CPIA Pub 330, Vol. 1 pg. 289.

4. R.A. Wires, J.P. Pfau, J.J. Rocchio, "The Effect of High Rates of Applied Force and Temperature on the Mechanical Properties of Gun Propellants", 1979 JANNAF Propulsion Meeting March 1979, CPIA Pub. 300 pg. 25.

5. S. Nicolaides, J. Pinto, and D.A. Wiegand, "Mechanical Properties, Mechanical Grain Failure, and Changes in the Burning Performance of Gun Propellant", 1980 JANNAF Propulsion Meeting, Monterey, CA CPIA Pub. 315, pg. 399.

6. H.W. Sandusky, W. L. Elban, K. Kim, R. R. Bernecker, S. B. Gross, and A. R. Clairmont, Jr. "Compaction of Porous Beds of Inert Materials", Seventh Detonation Symposium, Annapolis, MD June 16-19, 1981, Pg. 444.

7. K.K. Kuo, V. Yang, and B.B. Moore, "Intragranular Stress, Particle-Wall Friction, and Speed of Sound in Granular Propellant Beds", J. Ballistics Vol 4, pg. 697, 1980.

8. J. Pinto, D. Georgevich, S. Nicoliades, and D.A. Weigand, "Dynamic Mechanical Properties of Candidate LOVA and Nitrocellulose Base Gun Propellants After up to 18 Months of Accelerated (High Temperature) Aging." U.S. Army Armament Research and Development Center Technical Report ARLCD-TR-84006 (AD E 401171) May 1984.

9. Robert J. Lieb and Joseph J. Rocchio, "Standardization of a Drop Weight Mechanical Properties Tester for Gun Propellants". Ballistic Research Laboratory Technical Report ARBRL-TR-02516 July 1983.

10. S. Nicolaides, D.A. Weigand, and J. Pinto, "The Mechanical Behavior of Gun Propellant Grains in Interior Ballistics" June, 1982. U.S. Army Armament Research and Development Command Large Caliber Weapons Systems Technical Report ARLCD-TR-82010 (AD-F400 858). See also S. Nicolaides, D.A. Weigand, and J. Pinto, "The Mechanical Behavior of Gun Propellant Grains and its Role in Interior Ballistics" 16th JANNAF Structures and Mechanical Behavior Subcommittee Meeting, Colorado Springs, CO Dec 1979. CPIA Pub. 311 pg. 145.

11. M.S. Costantino, "Volumes and Sound Speeds of Two Gun Propellants at High Pressure", Propellants, Explosives and Pyrotechnics Vol. 9, pg. 22, 1984.

12. M.S. Costantino, "Uniaxial Strain Loading of a Porous Propellant", American Physical Society Topical Conference on Shock Waves In Condensed Matter, Santa Fe, NM July 18-21, 1983.

13. HIVELITE refers to a family of boron hydrogen fuel propellants. See, eg. M. Finger and B. Hayes, "Hivelite Propellant Characterization" Lawrence Livermore National Laboratory, Livermore, CA UCID-16748, 1975.

14. Charles Leveritt, Teledyne- McCormick-Selph, Personal communication.

15. A.A. Juhasz, I.W. May, W.P. Aungst, and F.R. Lynn, "Combustion Diagnostics of Very High Burning Rate Propellants" 17th JANNAF Combustion Meeting Hampton, VA 1980. CPIA Pub. 329 pg. 209.

16. E.B. Fisher, "One Dimensional Closed-Bomb Tests of Very High Burn Rate (VHBR) Propellants", Calspan Report No. 6744-D-1, June 1982.

17. D.E. Kooker and R.D. Anderson, "Progress in the Simulation of Hivelite Propellant Combustion" 19th JANNAF Combustion Meeting, NASA/GODDARD, Greenbelt, MD Oct. 1982.

18. Douglas E. Kooker and Ronald D. Anderson, "Closed Bomb Simulation of Hivelite Solid Propellant", 3rd JANNAF Propulsion Systems Hazards Meeting, Los Alamos, NM July 1983.

19. P.W. Bridgman, "The Pressure-Volume-Temperature relations of the liquid and the phase diagram of heavy water", J. Chem. Phys., Vol. 3, Pg. 597, 1935.

20. G.E. McDuffie, J.W. Forbes, W. M. Madigosky, and J.J. Von Bretzel, "Density and Compressibility of Four Higher Alcohols for Pressures to 2800 Kg. per sq. cm.", J. Chem. and Eng. Data., Vol. 14, pg. 176, 1969.

21. Walter M. Madigosky, "Instrument for Measuring Specific Volume as a Function of Pressure" Rev. Sci Instr. Vol. 37, Pg. 227, 1966.

22. G.C. Kennedy, W. L. Knight, and W.T. Holser, "Properties of Water. Part III. Specific Volume of Liquid Water to 100C and 1400 Bars", Am. J. Sci. Vol. 256 pg. 590, 1958.

23. C. Wayne Burnham, John R. Holloway, and Nicholas F. Davis, "Thermodynamic Properties of Water to 1,000°C and 10,000 Bars", The Geological Society of America Special Paper Number 132, 1969.

24. Handbook of Chemistry and Physics, 41st ed. pg. 2129.

25. P.W. Bridgman, "The Volume of Eighteen Liquids as a Function of Pressure and Temperature", Proc. Am. Acad. Arts Sci. Vol. 66 pg. 185, 1931.

26. International Mathmetics Software Library Subroutine ICSVKU. IMSL, NBC Building, 7500 Bellaire Blvd, Houston, TX 77036.

27. J.C. Jaeger and N.G.W. Cook, Fundamentals of Rock Mechanics, Chapman and Hall 1969. Chap. 4.